

Trends on band alignments: Validity of Anderson's rule in SnS₂- and SnSe₂-based van der Waals heterostructures

Daniel S. Koda,^{1,*} Friedhelm Bechstedt,^{2,†} Marcelo Marques,^{1,‡} and Lara K. Teles^{1,§}

¹*Grupo de Materiais Semicondutores e Nanotecnologia, Instituto Tecnológico de Aeronáutica, DCTA, 12228-900 São José dos Campos, Brazil*

²*Institut für Festkörpertheorie und -optik, Friedrich-Schiller-Universität, Max-Wien-Platz 1, D-07743 Jena, Germany*



(Received 16 January 2018; published 3 April 2018)

Van der Waals (vdW) heterostructures are promising candidates for building blocks in novel electronic and optoelectronic devices with tailored properties, since their electronic action is dominated by the band alignments upon their contact. In this work, we analyze 10 vdW heterobilayers based on tin dichalcogenides by first-principles calculations. Structural studies show that all systems are stable, and that commensurability leads to smaller interlayer distances. Using hybrid functional calculations, we derive electronic properties and band alignments for all the heterosystems and isolated two-dimensional (2D) crystals. Natural band offsets are derived from calculated electron affinities and ionization energies of 11 freestanding 2D crystals. They are compared with band alignments in true heterojunctions, using a quantum mechanical criterion, and available experimental data. For the hBN/SnSe₂ system, we show that hBN suffers an increase in band gap, while leaving almost unchanged the electronic properties of SnSe₂. Similarly, MX₂ (M = Mo, W; X = S, Se) over SnX₂ preserve the natural discontinuities from each side of the heterobilayer. Significant charge transfer occurs in junctions with graphene, which becomes p-doped and forms an Ohmic contact with SnX₂. Zirconium and hafnium dichalcogenides display stronger interlayer interactions, leading to larger shifts in band alignments with tin dichalcogenides. Significant orbital overlap is found, which creates zero conduction band offset systems. The validity of the Anderson electron affinity rule is discussed. Failures of this model are traced back to interlayer interaction, band hybridization, and quantum dipoles. The systematic work sheds light on interfacial engineering for future vdW electronic and optoelectronic devices.

DOI: 10.1103/PhysRevB.97.165402

I. INTRODUCTION

Driven by the growing family of two-dimensional (2D) crystals such as graphene (Gr), hexagonal boron nitride (hBN), transition metal dichalcogenides (TMDCs), group-IV (di)chalcogenides, and many others [1,2], the study of van der Waals (vdW) heterostructures [3,4] has emerged as one of the most active and exciting fields of research on the nanoscale. The interest is aroused by the manifold artificially stacked combinations of monolayer crystals with desired properties. The vdW heterostructures expand the range of tunable physical and chemical properties and allow for novel devices [3,4].

Heterojunctions are crucial elements in modern electronic, photonic, optoelectronic, and photovoltaic semiconductor technologies [5,6]. For instance, photovoltaic action for electron and hole separation requires type-II heterostructures [7] for light-harvesting [8], while light-emitting diodes benefit from a type-I band alignment [7] for a high emission efficiency [9]. Vertical tunneling field effect transistors (FETs) may count on (nearly) broken-gap alignment [7] for better performance [10]. vdW heterostructures based on atomically thin 2D crystals are fundamentally different and more flexible than those

based on conventional covalently bonded semiconductor interfaces. Their arrangement can be made with almost arbitrary order and orientation [3]. The lack of strong bonds between vdW materials enables for high-quality interfaces without the constraint of atomically precise commensurability [11–14]. Lattice mismatch, strain, interdiffusion, and interfacial defects play a minor role. These slight changes, however, may be crucial to obtain the properties of the interface as a whole.

The central electronic quantities for the action of a vdW heterojunction between two semiconducting 2D crystals are the band offsets or discontinuities between conduction and valence bands. They influence the transport and charge equilibrium processes of such interfaces [15–17]. Nevertheless, the majority of predictions are based on so-called natural band discontinuities between 2D crystals, mainly based on the original electron affinity rule [18,19], i.e., on the vacuum level alignment. The weak interlayer vdW bonding between two atomically thin crystals together leads to a low hybridization of electronic states [13,20] and the formation of quantum dipoles [21,22]. Most of the band offset studies have been done (i) for combinations of two TMDCs [15,16,23,24] and (ii) using *ab initio* calculations [16,23,24]. Heterostructures between 2D TMDCs and phosphorene [20,25], hBN [26], SnSe₂ [17], and SnS₂ [25] but also graphene/SnS₂ systems [27] are examples of combinations with potential applications.

The latter heterocombinations are in line with the rising interest in tin dichalcogenides SnS₂ and SnSe₂, which belong to the IVA-VIA family. These materials are earth-abundant and

*danielskoda@gmail.com

†friedhelm.bechstedt@uni-jena.de

‡mmarques@ita.br

§lkteles@ita.br

environmental friendly and, thus, have advantages in future nano- and optoelectronics [28,29]. With the improvement of techniques for the fabrication of 2D crystals of SnS_2 and SnSe_2 , several applications are being zealously studied [30]. Photodetectors with a fast response time of 42 ms made from 2D SnS_2 have been reported [31], as well as the high-performing version from SnSe_2 [28]. FETs with high on/off ratio have been demonstrated with SnS_2 nanomembranes [32], and increased carrier mobilities by 50 times for top-gated FETs based on monolayer SnS_2 on Al_2O_3 [33]. Their natural discontinuities also suggest the fabrication of tunneling FETs [17] and Esaki diodes [10]. Moreover, tin dichalcogenides are potential thermoelectric materials [34], and also serve as substrates to grow TMDCs [17,35] or SnS_2/Gr and $\text{SnS}_2/\text{reduced graphene oxide}$ composites [27], as well as phosphorene/ SnSe_2 [10] by means of vdW epitaxy.

In this paper, we exemplarily investigate 10 vdW heterostructures from first principles. These interfaces were constructed from combinations of tin dichalcogenides with graphene, hBN and a set of TMDCs, such as HfS_2 and MX_2 ($\text{M} = \text{Zr}, \text{Mo}, \text{W}$, and $\text{X} = \text{S}, \text{Se}$). We compare the natural band discontinuities resulting within the vacuum level alignment with those derived for the bilayer systems with a possible hybridization. Thereby, the necessary precision is reached by employing hybrid functionals for electronic structure calculations. The electron affinities and ionization energies computed for the isolated materials are used to derive chemical trends and to check the electron affinity rule. The results are compared with available experimental and theoretical data. Based on a systematic analysis, the possible failure of the Anderson rule in heterocombinations is then explained and extended to other 2D crystals. A general perspective for the validity of the Anderson rule in 2D heterostructures is presented. An important improvement in understanding of band offsets, interlayer interactions, and their role in vdW heterojunctions is made.

II. METHODOLOGY

Ground-state, structural, and electronic properties are calculated applying the density functional theory (DFT) as implemented in the Vienna *Ab initio* Simulation Package (VASP) [36,37] within the projector-augmented wave (PAW) method [38,39]. Exchange and correlation (XC) are described using the Perdew-Burke-Ernzerhof (PBE) functional within the generalized gradient approximation (GGA) [40]. Van der Waals interaction is taken into account via the optB86b functional [41] to minimize errors when predicting structural parameters and binding energies [41,42]. The kinetic energy cutoff for the plane-wave expansion is set as 500 eV. Integrations over the 2D Brillouin zone (BZ) are performed using a $12 \times 12 \times 1$ Γ -centered Monkhorst-Pack k -points mesh [43] for 1×1 lateral unit cells and supercells. The repeated slab method is applied to simulate individual and combined 2D crystals [44]. A vacuum of 15 Å thickness between the 2D crystals or heterobilayers is employed to avoid unphysical interaction in the stacking direction. The reference level for the electronic structures is adopted as the energy plateau in this vacuum region of the plane-averaged electrostatic potential for the isolated 2D crystals. However, since a charge transfer may occur in vdW heterostructures, dipole corrections are applied to satisfy the

periodic boundary conditions for the supercell in the stacking direction. This leads to the formation of two different vacuum levels, each relative to a side of the interface. Therefore, a step in the vacuum level is adopted for the interface, with height directly related to the magnitude of electrons transferred from one 2D crystal to the other.

Minimum lateral unit cells employed are found using the coincidence lattice method [13]. We make sure that the biaxial strain applied to the 2D crystals to make systems commensurate is smaller than 2% and that there are no more than 30 atoms inside the supercell. All structural parameters are calculated first finding the energy minimum with a stopping criterion of 10^{-5} eV for the energy convergence and then relaxing the atomic positions until the Hellmann-Feynman forces on atoms are smaller than 1 meV/Å. Heterostructure investigations are performed after fixing the parameters of the most stable structural geometry for each monolayer and applying necessary strains to make the systems commensurate.

Electronic properties calculated using the optB86b functional lead to an underestimation of energy gaps and interband distances since computed as differences of Kohn-Sham eigenvalues of the DFT [45]. They also lead to an incorrect description of hybridization and band offsets in vdW heterostructures [20]. To improve the quality of the investigation, we take approximate quasiparticle corrections into account by applying the XC hybrid functional HSE06 [45–48] to compute the electronic band structures and energy alignments. The fraction of exchange taken into account in the hybrid functional simulates the spatial nonlocality of the exchange-correlation self-energy in GW approximation. Consequently, the opening of gaps and interband transition energies with respect to the local or semilocal DFT may be interpreted as an approximate treatment of quasiparticle corrections [49].

III. RESULTS AND DISCUSSION

A. Isolated 2D crystals

We start from the optimized geometries of 11 freestanding 2D crystals listed in Fig. 1 to compute their natural band discontinuities calculated within the HSE06 approach [13]. All dichalcogenides are studied within their lowest-energy crystal structures, i.e., the 2H or 1T polytypes with space groups $\text{P}6_3/mmc$ and $\text{P}\bar{3}\text{m}1$, respectively, and flat honeycomb arrangements for Gr and hBN. Figure 1 depicts the conduction and valence band edges ε_c and ε_v of the selected set of isolated 2D crystals with respect to the vacuum level ε_{vac} . The absolute values give the electron affinities A and ionization energies I by

$$A = \varepsilon_{\text{vac}} - \varepsilon_c, \quad (1)$$

$$I = \varepsilon_{\text{vac}} - \varepsilon_v. \quad (2)$$

Their differences characterize the fundamental quasiparticle energy gaps

$$E_g = I - A. \quad (3)$$

Neglecting interface states, defect levels, charge transfer at a real interface, the Anderson's electron affinity rule [18,19,50]

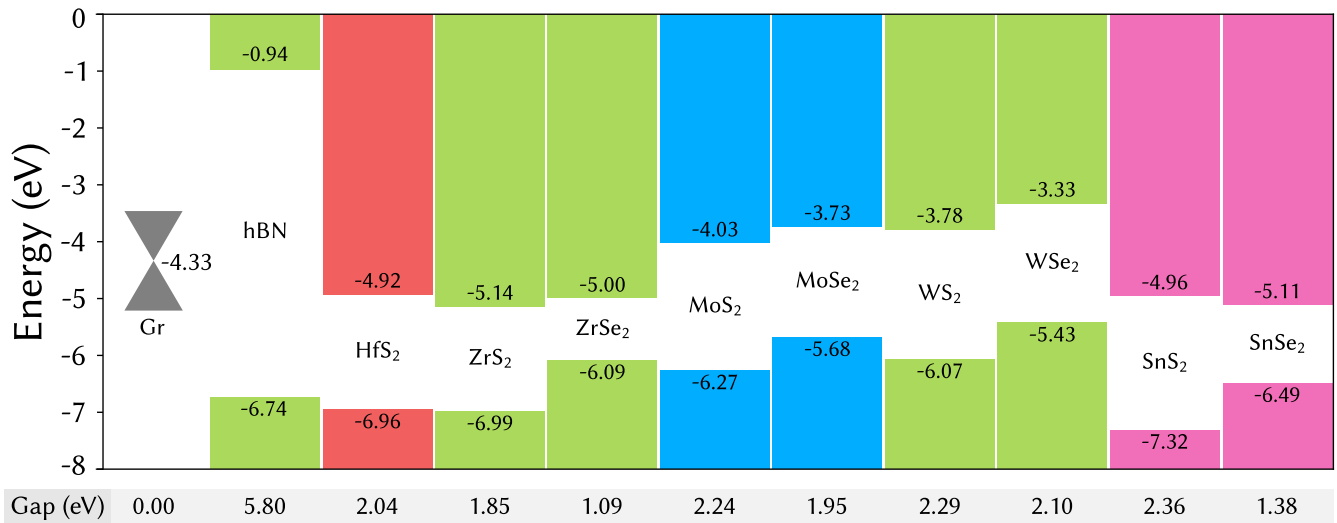


FIG. 1. Conduction and valence band edges calculated within HSE06 for the 2D crystals under study [13]. The colored bar edges represent the valence band maximum and the conduction band minimum for each monolayer, while the Dirac cone vertex characterizes the Fermi level for graphene. All energies are taken with respect to the vacuum level.

can be used to estimate the natural band discontinuities

$$\Delta E_c = A_1 - A_2, \quad (4)$$

$$\Delta E_v = I_2 - I_1 \quad (5)$$

with the 2D crystal 1 (2) on the left (right)-handed side of the heterobilayer.

Figure 1 shows clear chemical trends. With the increase of the anion size from S to Se, both the electron affinities and ionization energies decrease. The only exception appears comparing the conduction band edges of SnS₂ and SnSe₂. The quasiparticle gaps E_g of the dichalcogenides vary between 1.1 and 2.4 eV, indicating semiconducting behavior. The gap values, as well as the I and A values of freestanding 2D crystals, are comparable with those derived from one-shot GW calculations starting from DFT-PBE Kohn-Sham eigenvalues for MS₂ and MSe₂ (M = Zr, Mo, W) [27]. The GW gaps are slightly larger than the HSE06 ones because of the somewhat smaller (larger) A (I). However, the trends among the resulting natural band discontinuities from Eqs. (4) and (5) and their absolute values are rather similar. The observation of comparable band offsets in GW and HSE have been made also for other 2D materials [51]. For SnS₂ and SnSe₂, the gaps are slightly smaller than values for bulk 3D crystals from similar calculations [34] and much closer to the measured gaps of 2.07 and 0.97 eV [52]. The optical gap of SnSe₂ flakes on SiO₂/Si substrate has been measured to be 1.73 eV [28]. The work function of graphene $I = A = 4.33$ eV is in reasonable agreement with other theoretical [27,53] and experimental results [54]. The electron affinity, ionization energy, and fundamental gap reported for bulk SnS₂ and SnSe₂ [55] are also not too far from our computed values.

The variety of band alignments within the Anderson affinity rule demonstrate that the majority of heterostructures based on SnS₂ and SnSe₂ are from type II for the chosen crystals in Fig. 1 because of their large A and I values, at least for MoS₂, MoSe₂, WS₂, and WSe₂. For the WSe₂/SnSe₂ heterostructure, the type-

II finding is in agreement with photoemission data [17]. Only the “natural” values $\Delta E_c = 1.78$ eV and $\Delta E_v = -1.06$ eV are somewhat larger. Predictions for the heterojunctions of SnS₂ or SnSe₂ with HfS₂, ZrS₂, and ZrSe₂ are difficult, since the natural band offsets ΔE_c (SnS₂) and ΔE_v , as well as ΔE_c (SnSe₂), are small and may even vary with respect to the sign. For hBN, the situation is difficult since ΔE_v changes the sign with the anion in the dichalcogenide. While hBN/SnS₂ is a type-II system, hBN/SnSe₂ clearly shows a type-I character. Most interestingly is the formation of an ohmic contact between graphene and the tin chalcogenides, since this kind of interface is critical for low-resistance contacts for 2D electronic devices.

In summary, natural alignments, however, may be not enough to describe band offsets within vdW heterostructures. Hence, we simulate a series of combinations of 2D crystals in heterojunctions to predict and analyze systematically how stacking influences the band discontinuities.

B. Real heterostructures

To investigate the formation of interfaces between tin chalcogenides, graphene, boron nitride, and the selected TMDCs, we analyze favorable heterostructures. We apply the coincidence lattice method [13] to predict low-energy arrangements of the 2D systems with less than 2% of strain necessary to make an almost commensurate heterobilayer system and number of atoms up to 30 inside the supercell. Thereby, the lateral unit cells, as well as the rotation of the two crystals, are varied. The case of Gr/SnSe₂ is an exception, in which the system is forced to be commensurate at an angle of 0° to ensure a reasonable comparison with its SnS₂ counterpart. From then on, each heterostructure is constructed by applying an almost vanishing biaxial strain to the constituents, as given in Table I. We keep MoS₂, WS₂, MoSe₂, and WSe₂ unstrained due to their stiffness to biaxial strains when compared to SnS₂ and SnSe₂ [56]. Graphene is strained to preserve the electronic properties of SnS₂ and SnSe₂. In the other cases, the strain is distributed over both monolayers, compressive for one and

TABLE I. Combinations of 2D crystals with SnS_2 and SnSe_2 obtained using the coincidence lattice method. The layer 1/2 column relates the original monolayer unit cell to the supercell used in the heterostructure, denoted according to the Wood notation [57]. The first compound shown in the heterobilayer column is denoted as layer 1. The biaxial strains $\varepsilon_1/\varepsilon_2$ applied to the layers 1/2 to make the system commensurate also characterize the building of the supercell. The relaxed heterobilayer has an interlayer distance of d_{12} and a binding energy of E_b .

Heterobilayer	Layer 1	Layer 2	ε_1 (%)	ε_2 (%)	d_{12} (Å)	E_b (meV/Å ²)
Gr/SnS ₂	3×3	2×2	-0.91	0.00	3.38	20.1
HfS ₂ /SnS ₂	1×1	1×1	0.57	-0.56	2.97	21.1
MoS ₂ /SnS ₂	2×2	$(\sqrt{3} \times \sqrt{3}) \text{ R } 30.0^\circ$	0.00	-0.37	3.32	20.0
WS ₂ /SnS ₂	2×2	$(\sqrt{3} \times \sqrt{3}) \text{ R } 30.0^\circ$	0.00	0.20	3.34	18.7
ZrS ₂ /SnS ₂	1×1	1×1	0.23	-0.23	2.94	21.3
Gr/SnSe ₂	3×3	2×2	3.53	0.00	3.46	18.6
hBN/SnSe ₂	$(\sqrt{7} \times \sqrt{7}) \text{ R } 19.1^\circ$	$(\sqrt{3} \times \sqrt{3}) \text{ R } 30.0^\circ$	-0.08	0.08	3.42	18.3
MoSe ₂ /SnSe ₂	2×2	$(\sqrt{3} \times \sqrt{3}) \text{ R } 30.0^\circ$	0.00	-0.50	3.42	19.0
WSe ₂ /SnSe ₂	2×2	$(\sqrt{3} \times \sqrt{3}) \text{ R } 30.0^\circ$	0.00	-0.66	3.44	18.9
ZrSe ₂ /SnSe ₂	1×1	1×1	0.84	-0.82	3.00	22.2

tensile for the other. This strain distribution gives rise to small variations in electronic properties of the junctions. Then, the interlayer distance between the two layers is varied until an energy minimum is found. Finally, the system is relaxed to minimize atomic forces. The resulting binding energy E_b of the two layers is calculated as

$$E_b = \frac{(E_{\text{layer 1}} + E_{\text{layer 2}}) - E_{\text{het}}}{A_{\text{lateral cell}}}, \quad (6)$$

where $E_{\text{layer 1(2)}}$ is the total energy of the 2D crystal 1 (2) when isolated and correspondingly strained, E_{het} is the total energy of the relaxed heterostructure and $A_{\text{lateral cell}}$ is the area of the joint lateral unit cell.

For all investigated heterobilayers, stability is found and structural parameters are derived. In the 10 cases listed in Table I, the bilayers gain energy due to the interaction between the 2D crystals by vdW bonds, as demonstrated by the magnitude of the binding energy and the interlayer distance. As a rule of thumb, interlayer distances d_{12} around 3 Å are observed. The vdW binding E_b hardly varies around 20 meV/Å². For the particular HfS₂/SnS₂, ZrS₂/SnS₂, and ZrSe₂/SnSe₂ heterobilayers, the AA stacking is chosen to be simulated due to its enhanced stability and greater binding energy. This has been already shown for interfaces of HfS₂ and ZrS₂ [13] and explains the smaller interlayer distance of these systems within the trend as well. For the other systems, typical vdW distances and binding energies are achieved [13,20], as well as a spatial distribution of the bilayer stacking due to the supercell [20].

For the optimized structural parameters, we calculate electronic properties for all selected heterobilayers. Band structures for the heterobilayer systems are displayed in Fig. 2, in which the reference is taken as the largest vacuum potential for the interface. The bands are projected onto atomic sites and the contributions of an entire 2D layer is computed. This representation, depicted by markers with different colors in Fig. 2, allows us to determine the local energy gap and band discontinuities for each material in the heterostructure. The size of the markers is proportional to the contribution of each crystal to the joint band structure. Since the interface is atomically thin,

the band structure analyzed in the BZ determines the properties of the junction itself.

C. Band alignments

To predict the electronic properties of heterostructures for application in electronic and optoelectronic devices, it is indispensable to know the alignment of bands from one material to another. Using the projection technique described earlier and a criterion to determine band edges when hybridization is concerned [20], we plot the band diagrams for the heterobilayers. This allows us to understand, from a physical point of view, the relationship between the conduction band minima (CBMs) and valence band maxima (VBMs) from the isolated monolayers and the band offsets of the real interface. Figure 3 displays the energy diagrams of the studied vdW interfaces, together with their dipole potential step and isolated band schemes aligned via the vacuum level. Since a commensurability strain has been subject to the 2D crystals, we include the small shifts of the bands of the strained isolated monolayers into the energy diagrams. This allows us to decouple strain effects from the interlayer interactions and restrict our analysis solely to interfacial effects.

To derive chemical trends within the interface, the electronic structure results are displayed in Figs. 2 and 3. We start with the heterobilayers containing graphene, presenting a metallic behavior. Then we discuss the insulating hBN over SnSe₂, while finally discussing the semiconductor heterojunctions with TMDCs.

In the simulated Gr/SnS₂ and Gr/SnSe₂ vdW heterostructures, we first observe from Figs. 2(a) and 2(b) that the linear band dispersion of graphene is preserved in the heterobilayer system. The Gr Dirac cones, however, appear above the CBM of SnS₂ and SnSe₂. Therefore, these contacts give rise to significant charge transfers, creating a dipole potential of the order of 0.4 eV, leading to a vacuum level step and *p*-doping of the graphene layer. The two effects drastically change the work function of the bilayer, resulting in a metallic behavior. This work function modulation has been observed experimentally and reported in an earlier theoretical work [27]. In several devices, the formation of an ohmic contact, such as the one obtained for Gr/SnS₂ or Gr/SnSe₂, is preferred. The

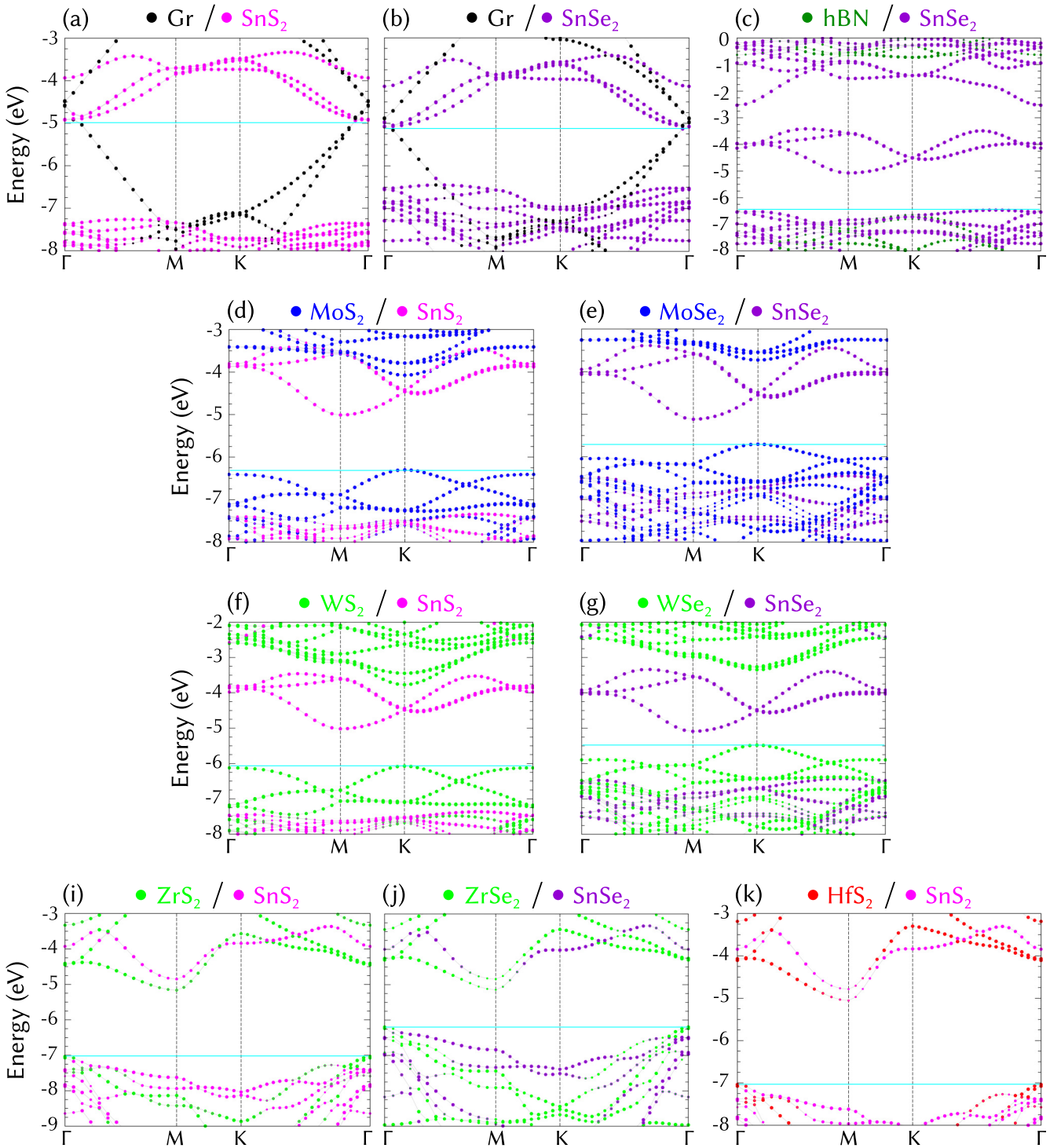


FIG. 2. Band structures calculated with HSE06 for 10 heterobilayers. The size of the marker represents the relative contribution of each monolayer to the eigenvalue, while its color depicts this contribution projected in the real space. The color representing each 2D crystal in the heterostructure is shown above the band structure. All energies are shown with respect to the highest vacuum level from each heterostructure. The top of the valence band for semiconductor systems (Fermi level for systems with graphene) is displayed with an horizontal light blue line.

rectification induced by a Schottky barrier is an impediment to create vdW heterostructure devices with good electric contacts. These interfaces present an alternative for manufacturing Ohmic contacts in 2D semiconductor devices [58].

Another 2D crystal used in vdW heterostructure devices is hBN. Its insulating properties make it useful for electric

barriers. By stacking a monolayer hBN on SnSe₂, we observe that the electronic properties of both materials are almost preserved, as displayed by the band structures in Fig. 2(c) and the band alignments of the systems in Fig. 3(c). Only minor changes are observed in the electronic properties of hBN. These modifications of the insulating substrate have

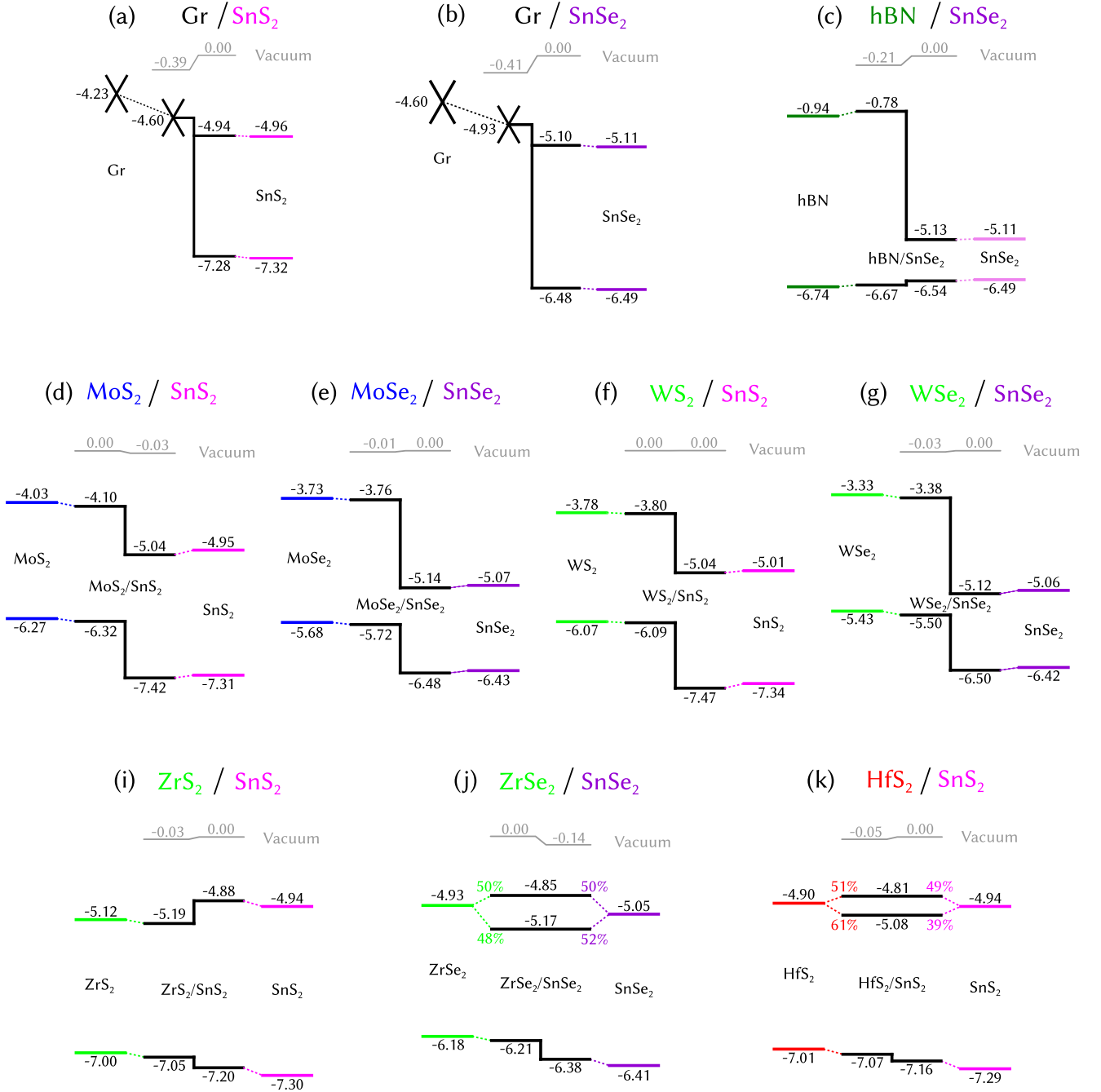


FIG. 3. Band alignments for each of the 10 heterobilayers under study. The natural band discontinuities for a 2D crystal are represented with colored lines, while the black solid lines at the center of each heterostructure diagram depict the heterojunction band offsets upon contact. The vacuum dipole step is shown in gray, and the colors of each material are specified within the legend of each diagram. In (j) and (k), a hybridization is found within the band edges, and the percentages represent the contribution of each monolayer to the formation of the band minima.

been also predicted for other TMDC/hBN interfaces [26] and experimentally observed for Gr/hBN heterostructures [59]. Although the hBN/SnSe₂ bilayer is a type-I heterostructure, its valence band offset (VBO) is pretty small in both approaches shown in Fig. 3(c). The large gap discontinuity $\Delta E_g = E_g^{\text{hBN}} - E_g^{\text{SnSe}_2}$ mainly results in a large conduction band offset (CBO), showing that the hole confinement on the SnSe₂ side is not very

effective. A mutual polarization of the two materials across the interface results in an electrostatic dipole. Its magnitude is compatible with those at interfaces with MoSe₂ [26].

SnS₂ and SnSe₂ have been largely used for vdW heterostructure devices as underlying substrate layer for the growth of TMDCs [35]. Hence, it is useful to understand the effects underlying the band alignments for these systems.

Heterostructures made by MoS₂ and WS₂ with SnS₂ show band offsets very close to their natural ones because of the vanishing interface dipole. The band offsets of $\Delta E_c = 0.9$ or 1.2 eV and $\Delta E_v = -1.1$ or -1.4 eV vary less than 0.1 eV when compared to the ones predicted by the strained monolayer situation. Thus, interfacial coupling almost preserves the local direct band gaps. Nevertheless, the joint electronic properties of the systems may indicate some changes, e.g., indirect band gaps in real space across the interface as for TMDC/SnS₂ systems. Only a small charge transfer occurs on the interface, as indicated by the vanishing vacuum step. These heterostructures are of type II for both MoS₂/SnS₂ and WS₂/SnS₂. The absolute values of ΔE_c and $|\Delta E_v|$ are of the order of 1 eV. This guarantees a spatial charge separation between the electrons and holes on the interface. Experimental results support our findings regarding the heterostructure type and interfacial coupling. Measurements for the stacked few-layer MoS₂, WS₂, and WSe₂ grown on SnS₂ microplates indeed indicate the existence of a weak interaction within the interface, leading even to a new peak in the photoluminescence spectrum [35]. In the case MoS₂ on SnS₂ this photoluminescence peak has been shown to be from electronic coupling and charge separation of MoS₂ and SnS₂ in the interface, suggesting a type-II heterostructure [60]. This fact is supported by the quenching of the strong excitonic emission peak of freestanding MoS₂.

Heterobilayers of MoSe₂ and WSe₂ on SnSe₂ are quite similar to the their sulfide analogous [see Figs. 3(e) and 3(g)]. Small changes are observed in the band alignments but still a vanishing dipole step is found, suggesting weak electronic polarization between the layers. Both heterostructures are of type II with band offsets of about $\Delta E_c = 1.4$ or 1.8 eV and $\Delta E_v = -0.8$ or -1.0 eV. However, the extremely small indirect gap between the WSe₂ VBM and the SnSe₂ CBM across the heterointerface almost tends to the properties of a broken-gap heterostructure. Experimental results agree with this heterostructure type predictions [17,61], with some differences in the reported offsets. Small discrepancies are found for the band gaps of WSe₂ and SnSe₂ when compared to measurements, ranging between 1.3 – 1.6 eV and 0.8 – 1.0 eV, respectively [17,61]. This is due to two facts: (i) the study of approximate quasiparticle gaps in contrast to the optical gaps from spectroscopic measurements and (ii) the dependence of the band gap of these 2D crystals on the number of atomic layers studied. Our results for a CBO of 1.8 eV and a VBO of 1.0 eV for the WSe₂/SnSe₂ interface slightly deviate from the experimental values. Excitonic bound states make the optical gaps smaller than the quasiparticle ones due to the strong exciton binding. It has to be eliminated to extract band offsets from optical data. Furthermore, experiments usually report data for few-layer crystals, such as a 3 – 6 WSe₂ layers [17]. The thickness influence and the excitonic effects make the results for the studied monolayer case slightly different from the experimental environment explored in the literature [17,61]. These effects explain the smaller CBO of 1.1 – 1.6 eV and a VBO of 0.8 eV for experimental studies [17,61] when compared to our results. Nevertheless, the vanishing gap at the WSe₂/SnSe₂ interface suggests application in tunneling field-effect transistors [17], while MoSe₂/SnSe₂ heterobilayers with pronounced type-II character may arouse interest for solar cells and high-performance field-effect transistors [62].

Most interestingly are the HfS₂/SnS₂, ZrS₂/SnS₂ and ZrSe₂/SnSe₂ heterostructures when phenomena at the band edges are considered. Due to the small lattice mismatch of these systems ($<2\%$), it is possible to simulate them as commensurate 1×1 systems by applying a biaxial strain to the crystals. This is not unrealistic though, since similar constraints have been observed experimentally for other vdW heterostructures [63]. This kind of commensurability have also been enforced while modulating the interlayer distance between the 2D crystals [64].

The three heterojunctions in Figs. 3(i), 3(j), and 3(k) have stacking patterns which lead to different stabilities [13,65]. We investigate the most stable of them, namely, the AA stacking. The smallest interlayer distances among the studied systems below 3 Å (see Table I) lead to stronger binding energies E_b . This distance decrease is related to stronger interlayer interaction and orbital overlap, which may also tune the electronic properties of the materials, especially their band gaps and band offsets, e.g., by the piezoelectric effect [20,66,67]. In the ZrSe₂/SnSe₂ and HfS₂/SnS₂ heterostructures, for example, the wave function overlap drastically changes the lowest conduction bands of the heterojunctions. The almost degenerate states forming the conduction band edges are lifted. According to the molecular orbital theory, the hybridization of the band states of opposite layers in this contact leads to two different energy levels related to bonding and antibonding combinations. Since both layers have a significant contribution to the formation of the joint conduction bands, the definition of a CBO is difficult. In a quantum mechanical sense, the electrons in these bands are delocalized throughout the interface. This fact suggests to derive a zero CBO for these systems. Electrons can freely move in any direction without facing an energy barrier. Other calculations for a HfSe₂/SnS₂ heterostructure [68] are in agreement with our results. On the other hand, in Figs. 2(i) and 3(i), the ZrS₂/SnS₂ junction exhibits only a weak hybridization when compared to its counterparts shown in Figs. 3(j) and 3(k). The conduction band minimum is formed by 70% of ZrS₂ contributions, which allow a proper definition of a band offset using the quantum mechanical criterion of the highest probability to find an electron on one side of the heterointerface [20].

By projecting the band structures under investigation onto atomic orbitals, it is possible to analyze the composition of the electronic structures for each k point. From this information, we observe how the spatial distribution of atomic orbitals influences the band edges upon contact with other layers. While the conduction band is modified by a strong hybridization between the 2D crystals, at least in the latter cases, the uppermost valence band of these three heterosystems is only slightly affected. This is due to the fact that the in-plane orbitals p_x and p_y from the sulfur and selenium anions, responsible for the formation of the valence bands of all five monolayers constituting the three heterointerfaces, remain unaffected upon contact between the layers. By contrast, the conduction bands of ZrS₂, ZrSe₂, and HfS₂ are composed mainly by d_{z^2} , d_{xz} , and d_{yz} orbitals from the metal atom and p_z orbitals from the anion, and tend to hybridize upon out-of-plane contacts. The corresponding orbital-projected band structures for these TMDC are found in Ref. [13]. The conduction bands of SnS₂ and SnSe₂ are composed mainly by spherically symmetric s orbitals and, therefore, are hardly influenced by the neighboring layers.

D. Anderson rule

In addition to the explicit band alignments given in Fig. 3, the formulation of trends is necessary. A heuristic technique commonly applied to semiconductor interfaces is the electron affinity rule, known as the Anderson rule [18,19]. According to this rule, the CBO in a semiconductor heterojunction has to be taken directly from the difference between the electron affinities, while the VBO is obtained by the CBO and the quasiparticle (not optical) band gaps of the materials [Eq. (3)]. In three-dimensional semiconductor heterostructures, stronger mixed covalent-ionic chemical bonding occurs at the interface, which turns the Anderson rule into a rough approximation to describe the junction [50]. On the other hand, since weak vdW interaction is responsible for the stability of vdW stacks of 2D crystals, the electron affinity rule should be fulfilled for these heterostructures [69]. Based on our results, we analyze this expectation in detail below.

We start with cases in which the electron affinity rule in Eq. (4) is obviously fulfilled, i.e., where the band alignment in the heterostructure (central part of each panel in Fig. 3) can be explained by the “natural” band positions (left and right parts of each panel). The superposition of group VIB metal dichalcogenides, such as MX_2 ($\text{M} = \text{Mo}, \text{W}$ and $\text{X} = \text{S}, \text{Se}$) with SnX_2 , nearly preserves the natural band alignments, with shifts smaller than 0.1 eV in the real heterojunctions. The small dipole potential step in the interface indicates a small charge transfer between the monolayers. The lattice mismatch between the original 1×1 Bravais lattices up to 15% and the difference between their polymorphs (2H for the TMDCs, 1T for the tin dichalcogenides [13]) are impediments to a commensurate 1×1 stacking. The extremely dense coincidence lattices also lead to small interlayer distances. Despite the maximum coincidence and the almost vanishing strain (see Table I), interlayer interactions are hindered due to the larger distances between the layers. The chemically dissimilar band compositions leave the monolayers almost intact. Small amounts of charge transfers are found, forming only vanishing dipole steps in the vacuum level (see Fig. 3).

When hBN is put into contact with SnSe_2 , the heterostructure CBO = 4.4 eV differs from the natural CBO $\Delta E_c = 4.2$ eV, using the electron affinity rule, by almost 0.2 eV. Although no impact is observed on the electronic properties of SnSe_2 , the insulating hBN layer has modified band edges upon the contact. The large gap of hBN hinders hybridization between the layers, even if its band edge orbital character is mainly p_z on both sides of the interface. The large CBO keeps the SnSe_2 CBM almost identical to the one observed in the monolayer case, while the VBM from both crystals suffer from the small VBO. While the electron affinity rule is a reasonable approximation for systems such as the hBN/ SnSe_2 one, it does not account for the physical interaction across the interface.

In the case of graphene on SnX_2 the Anderson rule is violated by about 0.4 eV, because of the metallic behavior of the heterostructures. Since the Fermi level of undoped monolayer graphene is above the CBM for both tin dichalcogenides under investigation, a large amount of charge is transferred. In both cases, the p -doping of graphene is responsible for drastic shifts in band alignments.

Also, heterostructures made with group IV-B TMDCs and SnX_2 violate the Anderson rule, even although crystals are only weakly bonded by vdW interaction. One observes a strong hybridization resulting in vanishing CBOs in two cases. This fact seems to be in contrast to the simplicity of the atomic geometries of these heterointerfaces. These heterostructures are made by almost lattice-matched 2D crystals (see Table I). Therefore, they can be simulated as 1×1 commensurate systems, leading to small interlayer distances for the AA stacking. This small interlayer distance enhances the conduction state hybridization and dramatically changes the electronic properties of the studied heterosystems. This also happens in the case of phosphorene combined with TMDCs [20].

To validate the above hypothesis, we simulate the same three heterostructures, with exactly the same stacking, but with a larger interlayer distance. Compared to the equilibrium distances d_{12} in Table I, the interlayer distances are increased to values above 3 Å, to 3.32 Å for $\text{HfS}_2/\text{SnS}_2$, 3.34 Å for $\text{ZrS}_2/\text{SnS}_2$ and 3.41 Å for $\text{ZrSe}_2/\text{SnSe}_2$. The electronic properties are calculated again using the same methodology. The resulting band alignments are displayed in Fig. 4. Comparing these results with those for the most stable arrangements, the vanishing dipole potential steps in Fig. 4 and hybridization-induced splittings of the conduction bands for $\text{ZrSe}_2/\text{SnSe}_2$ show that the electron affinity rule is indeed better fulfilled for the zirconium-based dichalcogenides on top of tin-based dichalcogenides. The increase of the interlayer distance reduces the vdW interaction and hybridization between both layers. The zero CBO in the equilibrium $\text{ZrSe}_2/\text{SnSe}_2$ heterostructure is replaced by a well-defined CBO for larger interlayer distance in heterostructures. Each 2D crystal hybridizes less with the other layer, leading to 69% SnSe_2 contribution to the formation of the joint conduction band. Shifts of about 0.05 eV in the conduction band edges are related to the lift of band degeneracy and the accompanying reduction of hybridization. These effects cannot be ignored in the equilibrium vdW heterostructures, as in the case of $\text{HfS}_2/\text{SnS}_2$. Comparing Fig. 4(c) with Fig. 3(k), we observe that the shifts in the valence band almost vanish when a larger interlayer distance is applied to the system. However, contrary to what is observed in the heterostructures of zirconium and tin dichalcogenides, the CBO does not vanish in the $\text{HfS}_2/\text{SnS}_2$ case. The conduction band edges still shift with respect to the situation in the isolated cases. The increase of the interlayer distance, nevertheless, decreases the interlayer interaction. In the three cases studied, the magnitude of charge transfer is smaller, as evidenced by the almost zero dipole step in the vacuum potential.

The results of our analysis are in agreement with the requirements of the Anderson rule [50]. For the 2D bilayer heterostructures, we highlighted the three main requirements for the validity of the rule: (i) the orbital overlap should be negligible; (ii) the interlayer interaction should vanish and not be enhanced by external influences, such as electric fields or pressure; and (iii) the natural band positions should be energetically far from each other, so that state hybridization across the interface is suppressed upon the contact. In summary, there is a clear tendency that the Anderson rule is fulfilled for vdW bilayer heterostructures with an accuracy of about 0.1 eV.

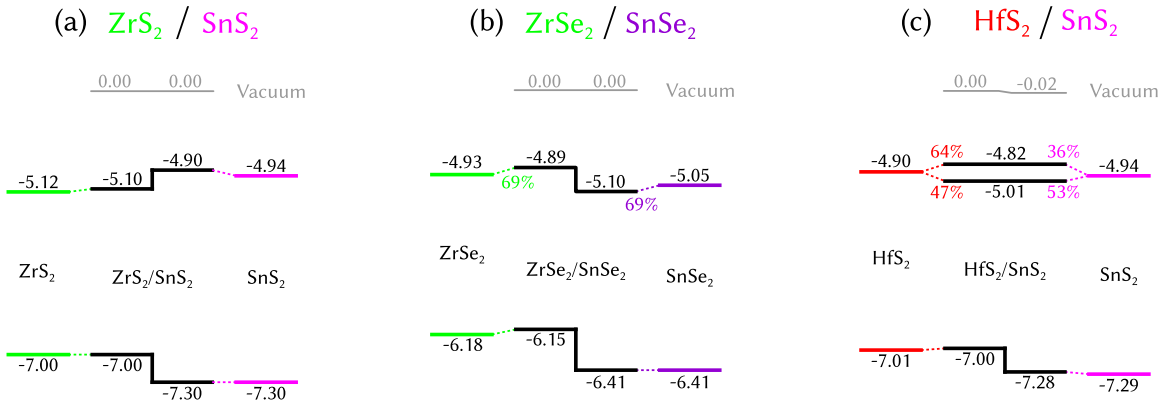


FIG. 4. Band alignments for (a) $\text{ZrS}_2/\text{SnS}_2$, $\text{ZrSe}_2/\text{SnSe}_2$, and $\text{HfS}_2/\text{SnS}_2$ heterostructures with increased interlayer separation (see text). Colored solid lines depict the natural band discontinuities from each monolayer, while the solid black lines represent the band discontinuities upon contact of the systems. The percentage represents the relative contribution of each monolayer to the formation of the band indicated.

However, in cases where band states localized at opposite sides of the heterointerface are almost energetically degenerate, strong hybridization effects may occur. The accompanying band splittings may violate the rule. This knowledge on vdW bilayer heterostructures may help the band structure engineering for 2D electronic and optoelectronic devices.

IV. SUMMARY AND CONCLUSIONS

In summary, we have simulated ten different tin dichalcogenides-based vdW heterostructures made from 11 different 2D crystals by first-principles calculations. We found atomic geometries for the heterobilayers which minimizes the total energy within the DFT, showing that all systems are stable upon contact and that the interlayer distance between the systems tends to the commensurability of the stack for increased lateral unit cells. Using the hybrid functional HSE06 functional, electronic structures are calculated for all heterosystems. From them, band alignments have been derived and compared to their natural band offsets, obtained by vacuum-level alignment and measurements, showing good agreement. Trends among these heterointerfaces have been observed, and their potential applications to device fabrication are emphasized.

An Ohmic contact is formed between graphene and SnX_2 ($X = \text{S}, \text{Se}$), leading to a *p*-doping of the graphene layer. The insulating properties of hBN are slightly changed upon contact with SnSe_2 , while the latter remains almost unchanged. Molybdenum and tungsten dichalcogenides underly small variations, such as band shifts with respect to their isolated monolayer band edges, when stacked over SnX_2 , but their band offsets are mostly unaffected. Zirconium dichalcogenides and HfS_2 over SnX_2 interact more strongly with each other, leading to larger shifts in the band offsets between the layers and an

important orbital overlap, which gives rise to a zero conduction band offset in the most stable stacking.

We also investigated the validity of the electron affinity rule, which works quite accurately for all studied systems except for group-IVB TMDCs on monolayer SnX_2 substrates. In latter cases, we investigated the effect of the interlayer separation, demonstrating that the commensurability of the systems play an important role in the interlayer interaction and state hybridization between the 2D crystals. The increase of the interlayer separation changes the band offsets toward the natural band discontinuities and reduces the hybridization between the layers. We observed an important feature regarding the degeneracy of energy levels, demonstrating its capability to shift the conduction band minimum of the heterobilayer system by the hybridization-induced band splitting. The knowledge of trends on band alignments and electronic properties of bilayers, as well as the almost validity of the Anderson rule for the studied cases, may guide the way for predicting the action of novel electronic and optoelectronic devices.

ACKNOWLEDGMENTS

The authors acknowledge the National Laboratory for Scientific Computing (LNCC/MCTI, Brazil) for providing HPC resources of the SDumont supercomputer, which have contributed to the electronic structures reported within this paper, and CENAPAD-SP, in which structural calculations have been performed. This work was funded by the Brazilian agencies Fundação de Amparo à Pesquisa do Estado de São Paulo (Grant No. 2012/50738-3), Conselho Nacional de Desenvolvimento Científico e Tecnológico (Grants No. 305405/2014-4 and No. 308742/2016-8) and Coordenação de Aperfeiçoamento de Pessoal de Nível Superior (Programa Professor Visitante do Exterior, Grant No. 88881.068355/2014-01 and scholarship grant) within the program Science Without Borders.

[1] S. Z. Butler, S. M. Hollen, L. Cao, Y. Cui, J. A. Gupta, H. R. Gutiérrez, T. F. Heinz, S. S. Hong, J. Huang, A. F. Ismach, E. Johnston-Halperin, M. Kuno, V. V. Plashnitsa, R. D. Robinson, R. S. Ruoff, S. Salahuddin, J. Shan, L. Shi, M. G. Spencer, M.

Terrones, W. Windl, and J. E. Goldberger, *ACS Nano* **7**, 2898 (2013).

[2] X. Li, L. Tao, Z. Chen, H. Fang, X. Li, X. Wang, J.-B. Xu, and H. Zhu, *Appl. Phys. Rev.* **4**, 021306 (2017).

- [3] A. Geim and I. Grigorieva, *Nature* **499**, 419 (2013).
- [4] K. S. Novoselov, A. Mishchenko, A. Carvalho, and A. H. Castro Neto, *Science* **353**, aac9439 (2016).
- [5] H. Kroemer, *Rev. Mod. Phys.* **73**, 783 (2001).
- [6] M.-L. Tsai, S.-H. Su, J.-K. Chang, D.-S. Tsai, C.-H. Chen, C.-I. Wu, L.-J. Li, L.-J. Chen, and J.-H. He, *ACS Nano* **8**, 8317 (2014).
- [7] C. Kittel, *Introduction to Solid State Physics*, 8th ed. (Wiley, Hoboken, 2004).
- [8] Y. J. Song, M. Park, E. Gulians, and W. A. Anderson, *Sol. Energy Mater. Sol. Cells* **64**, 225 (2000).
- [9] P. Waltereit, O. Brandt, A. Trampert, H. T. Grahn, J. Menniger, M. Ramsteiner, M. Reiche, and K. H. Ploog, *Nature* **406**, 865 (2000).
- [10] R. Yan, S. Fathipour, Y. Han, B. Song, S. Xiao, M. Li, N. Ma, V. Protasenko, D. A. Muller, D. Jena, and H. G. Xing, *Nano Lett.* **15**, 5791 (2015).
- [11] M. Chhowalla, H. S. Shin, G. Eda, L.-J. Li, K. P. Loh, and H. Zhang, *Nat. Chem.* **5**, 263 (2013).
- [12] C.-H. Lee, G.-H. Lee, A. M. Van Der Zande, W. Chen, Y. Li, M. Han, X. Cui, G. Arefe, C. Nuckolls, T. F. Heinz, J. Guo, J. Hone, and P. Kim, *Nat. Nanotechnol.* **9**, 676 (2014).
- [13] D. S. Koda, F. Bechstedt, M. Marques, and L. K. Teles, *J. Phys. Chem. C* **120**, 10895 (2016).
- [14] G. Argentero, A. Mittelberger, M. Reza Ahmadpour Monazam, Y. Cao, T. J. Pennycook, C. Mangler, C. Kramberger, J. Kotakoski, A. Geim, and J. C. Meyer, *Nano Lett.* **17**, 1409 (2017).
- [15] X. Hong, J. Kim, S.-F. Shi, Y. Zhang, C. Jin, Y. Sun, S. Tongay, J. Wu, Y. Zhang, and F. Wang, *Nat. Nanotechnol.* **9**, 682 (2014).
- [16] X. Zhu, N. R. Monahan, Z. Gong, H. Zhu, K. W. Williams, and C. A. Nelson, *J. Am. Chem. Soc.* **137**, 8313 (2015).
- [17] T. Roy, M. Tosun, M. Hettick, G. H. Ahn, C. Hu, and A. Javey, *Appl. Phys. Lett.* **108**, 083111 (2016).
- [18] R. Anderson, *Solid-State Electron.* **5**, 341 (1962).
- [19] R. Anderson, *IBM J. Res. Dev.* **4**, 283 (1960).
- [20] D. S. Koda, F. Bechstedt, M. Marques, and L. K. Teles, *J. Phys. Chem. C* **121**, 3862 (2017).
- [21] J. Tersoff, *Phys. Rev. B* **30**, 4874 (1984).
- [22] R. Schlaf, O. Lang, C. Pettenkofer, W. Jaegermann, and N. Armstrong, *J. Vac. Sci. Technol. A* **15**, 1365 (1997).
- [23] J. Kang, S. Tongay, J. Zhou, J. Li, and J. Wu, *Appl. Phys. Lett.* **102**, 012111 (2013).
- [24] M.-H. Chiu, C. Zhang, H.-W. Shiu, C.-P. Chuu, C.-H. Chen, C.-Y. S. Chang, C.-H. Chen, M.-Y. Chou, C.-K. Shih, and L.-J. Li, *Nat. Commun.* **6**, 7666 (2015).
- [25] V. D. S. Ganesan, J. Linghu, C. Zhang, Y. P. Feng, and L. Shen, *Appl. Phys. Lett.* **108**, 122105 (2016).
- [26] D. S. Koda, F. Bechstedt, M. Marques, and L. K. Teles, *J. Electron. Mater.* **46**, 3910 (2017).
- [27] C. S. Rout, P. D. Joshi, R. V. Kashid, D. S. Joag, M. A. More, A. J. Simbeck, M. Washington, S. K. Nayak, and D. J. Late, *Appl. Phys. Lett.* **105**, 043109 (2014).
- [28] X. Zhou, L. Gan, W. Tian, Q. Zhang, S. Jin, H. Li, Y. Bando, D. Golberg, and T. Zhai, *Adv. Mater.* **27**, 8035 (2015).
- [29] M. Filsø, E. Eikeland, J. Zhang, S. Madsen, and B. Iversen, *Dalton Trans.* **45**, 3798 (2016).
- [30] X. Zhou, Q. Zhang, L. Gan, H. Li, J. Xiong, and T. Zhai, *Adv. Sci.* **3**, 1600177 (2016).
- [31] J. Xia, D. Zhu, L. Wang, B. Huang, X. Huang, and X.-M. Meng, *Adv. Funct. Mater.* **25**, 4255 (2015).
- [32] D. De, J. Manongdo, S. See, V. Zhang, A. Guloy, and H. Peng, *Nanotechnology* **24**, 025202 (2012).
- [33] H. Song, S. Li, L. Gao, Y. Xu, K. Ueno, J. Tang, Y. Cheng, and K. Tsukagoshi, *Nanoscale* **5**, 9666 (2013).
- [34] B.-Z. Sun, Z. Ma, C. He, and K. Wu, *Phys. Chem. Chem. Phys.* **17**, 29844 (2015).
- [35] X. Zhang, F. Meng, J. R. Christianson, C. Arroyo-Torres, M. A. Lukowski, D. Liang, J. R. Schmidt, and S. Jin, *Nano Lett.* **14**, 3047 (2014).
- [36] G. Kresse and J. Furthmüller, *Comput. Mat. Sci.* **6**, 15 (1996).
- [37] G. Kresse and J. Furthmüller, *Phys. Rev. B* **54**, 11169 (1996).
- [38] P. E. Blöchl, *Phys. Rev. B* **50**, 17953 (1994).
- [39] G. Kresse and D. Joubert, *Phys. Rev. B* **59**, 1758 (1999).
- [40] J. P. Perdew, K. Burke, and M. Ernzerhof, *Phys. Rev. Lett.* **77**, 3865 (1996).
- [41] J. Klimeš, D. R. Bowler, and A. Michaelides, *Phys. Rev. B* **83**, 195131 (2011).
- [42] T. Björkman, *J. Chem. Phys.* **141**, 074708 (2014).
- [43] H. J. Monkhorst and J. D. Pack, *Phys. Rev. B* **13**, 5188 (1976).
- [44] F. Bechstedt, *Principles of Surface Physics* (Springer-Verlag, Berlin/Heidelberg, 2003).
- [45] J. Paier, M. Marsman, K. Hummer, G. Kresse, I. C. Gerber, and J. G. Ángyán, *J. Chem. Phys.* **124**, 154709 (2006).
- [46] J. Paier, M. Marsman, K. Hummer, G. Kresse, I. Gerber, and J. Ángyán, *J. Chem. Phys.* **125**, 249901 (2006).
- [47] J. Heyd, G. E. Scuseria, and M. Ernzerhof, *J. Chem. Phys.* **118**, 8207 (2003).
- [48] J. Heyd, G. E. Scuseria, and M. Ernzerhof, *J. Chem. Phys.* **124**, 219906 (2006).
- [49] F. Bechstedt, *Many-Body Approach to Electronic Excitations* (Springer-Verlag, Berlin/Heidelberg, 2015).
- [50] F. Bechstedt and R. Enderlein, *Semiconductor Surfaces and Interfaces: Their Atomic and Electronic Structures*, Physical Research (Akademie-Verlag, Berlin, 1988).
- [51] Y. Liang, S. Huang, R. Soklaski, and L. Yang, *Appl. Phys. Lett.* **103**, 042106 (2013).
- [52] G. Domingo, R. Itoga, and C. Kannewurf, *Phys. Rev.* **143**, 536 (1966).
- [53] G. Giovannetti, P. A. Khomyakov, G. Brocks, V. M. Karpan, J. van den Brink, and P. J. Kelly, *Phys. Rev. Lett.* **101**, 026803 (2008).
- [54] C. Oshima and A. Nagashima, *J. Phys.: Condens. Matter* **9**, 1 (1997).
- [55] J. Robertson, *J. Phys. C: Solid State Phys.* **12**, 4753 (1979).
- [56] D. M. Guzman and A. Strachan, *J. Appl. Phys.* **115**, 243701 (2014).
- [57] E. A. Wood, *J. Appl. Phys.* **35**, 1306 (1964).
- [58] A. Allain, J. Kang, K. Banerjee, and A. Kis, *Nat. Mater.* **14**, 1195 (2015).
- [59] M. Pan, L. Liang, W. Lin, S. M. Kim, Q. Li, J. Kong, M. S. Dresselhaus, and V. Meunier, *2D Mater.* **3**, 045002 (2016).
- [60] B. Li, L. Huang, M. Zhong, Y. Li, Y. Wang, J. Li, and Z. Wei, *Adv. Electron. Mater.* **2**, 1600298 (2016).
- [61] K. E. Aretouli, D. Tsoutsou, P. Tsipas, J. Marquez-Velasco, S. Aminalragia Giannini, N. Kelaidis, V. Pscharis, and A. Dimoulas, *ACS Appl. Mater. Interfaces* **8**, 23222 (2016).

- [62] P. Chen, J. Shang, Y. Yang, R. Wang, and X. Cheng, *Appl. Surf. Sci.* **419**, 460 (2017).
- [63] C. R. Woods, L. Britnell, A. Eckmann, R. S. Ma, J. C. Lu, H. M. Guo, X. Lin, G. L. Yu, Y. Cao, R. V. Gorbachev, A. V. Kretinin, J. Park, L. A. Ponomarenko, M. I. Katsnelson, Y. N. Gornostyrev, K. Watanabe, T. Taniguchi, C. Casiraghi, H.-J. Gao, A. K. Geim, and K. S. Novoselov, *Nat. Phys.* **10**, 451 (2014).
- [64] M. Yankowitz, K. Watanabe, T. Taniguchi, P. San-Jose, and B. J. LeRoy, *Nat. Commun.* **7**, 13168 (2016).
- [65] K. Kośmider and J. Fernández-Rossier, *Phys. Rev. B* **87**, 075451 (2013).
- [66] H. Zhu, Y. Wang, J. Xiao, M. Liu, S. Xiong, Z. J. Wong, Z. Ye, Y. Ye, X. Yin, and X. Zhang, *Nat. Nanotechnol.* **10**, 151 (2014).
- [67] W. Wu, L. Wang, Y. Li, F. Zhang, L. Lin, S. Niu, D. Chenet, X. Zhang, Y. Hao, T. F. Heinz, J. Hone, and Z. L. Wang, *Nature* **514**, 470 (2014).
- [68] S. Su, P. Das, S. Ge, and R. K. Lake, *J. Chem. Phys.* **146**, 064701 (2017).
- [69] M.-H. Chiu, W.-H. Tseng, H.-L. Tang, Y.-H. Chang, C.-H. Chen, W.-T. Hsu, W.-H. Chang, C.-I. Wu, and L.-J. Li, *Adv. Funct. Mater.* **27** 1603756 (2017).